

# Short-Time Effects on Eigenstate Structure in Sinai Billiards and Related Systems

L. Kaplan\*

Department of Physics and Society of Fellows,  
Harvard University, Cambridge, MA 02138

E. J. Heller†

Department of Physics and Department of Chemistry,  
Harvard University, Cambridge, MA 02138

There is much latitude between the requirements of Schnirelman's theorem regarding the ergodicity of individual high-energy eigenstates of classically chaotic systems on the one hand, and the extreme requirements of random matrix theory on the other. It seems likely that some eigenstate statistics and long-time transport behavior bear nonrandom imprints of the underlying classical dynamics while simultaneously obeying Schnirelman's theorem. Indeed this was shown earlier in the case of systems which approach classical ergodicity slowly, and is also realized in the scarring of eigenstates, even in the  $\hbar \rightarrow 0$  limit, along unstable periodic orbits and their manifolds. Here we demonstrate the nonrandom character of eigenstates of Sinai-like systems. We show that mixing between channels in Sinai systems is dramatically deficient compared to random matrix theory predictions. The deficit *increases* as  $|\log \hbar|$  for  $\hbar \rightarrow 0$ , and is due to the vicinity of the measure zero set of orbits which never collide with the Sinai obstruction. Coarse graining to macroscopic scales recovers the Schnirelman result. Three systems are investigated here: a Sinai-type billiard, a quantum map which possesses the essential properties of the Sinai billiard, and a unitary map corresponding to a quasirandom Hamiltonian. Various wavefunction and long-time transport statistics are defined, theoretically investigated, and compared to numerical data.

## I. INTRODUCTION

In recent years, much attention has been paid to the structure of quantum eigenstates in systems with a chaotic or ergodic classical analogue. For integrable systems, EBK quantization provides an intuitive understanding of classical-quantum correspondence, associating quantum wavefunctions with the invariant tori of the underlying classical dynamics. In a classically ergodic system, the typical trajectory fills an entire energy hypersurface at long times, and it is natural to conjecture that a typical high-energy eigenstate of such a system similarly has intensity distributed evenly over an entire energy shell. Thus, Berry suggested in 1983 that an eigenstate of a classically ergodic system should look locally

like a random superposition of plane waves of fixed energy, with momenta pointing in all possible directions [1]. Similarly, Bohigas, Giannoni, and Schmit [2] proposed that the quantum properties of a classically chaotic system should correspond to those of random matrix theory (RMT). This implies that wavefunction intensity should be distributed over an entire energy surface, with the wavefunction amplitudes at distant points behaving as independent Gaussian variables.

The conjecture that chaotic eigenstates obey RMT statistics is a statement about quantum structure at the scale of a single wavelength in position space (or on the scale of a single channel in momentum space, or more generally, on a mesh of cell size  $O(\hbar)$  in phase space). Rigorous results on quantum ergodicity, however, mostly address structure on classically large scales, in the limit where  $\hbar$  becomes small compared to the phase-space region over which wavefunction intensity is being smoothed. Specifically, theorems by Schnirelman, Zelditch, and Colin de Verdiere (SZCdV) [3] state that for a classically defined operator, the expectation value over almost all wavefunctions converges to the microcanonical average of the classical version of the operator, in the  $\hbar \rightarrow 0$  limit. Since the classical symbol of the operator is kept fixed as the limit is taken, these theorems provide information only about the coarse-grained structure of the eigenstates, and not about the structure at quantum mechanical scales.

Wavefunction scarring, the anomalous enhancement (or suppression) of intensity near an unstable periodic orbit, is a well-known example of non-RMT behavior of eigenstates in a classically chaotic system. The distribution of wavefunction intensities on a fixed periodic orbit can be computed in the semiclassical limit using the linear and nonlinear theory of scars [4–6], and is found to be very different from the Porter-Thomas prediction of RMT. Furthermore, upon ensemble averaging, a power-law wavefunction intensity distribution tail is obtained (and numerically observed) in chaotic systems, in contrast with the exponential falloff prediction of RMT. The fraction of strongly scarred states remains finite in the  $\hbar \rightarrow 0$  limit. Nevertheless, scarring poses no threat to the SZCdV ergodicity condition, because the size of the scarred phase-space region surrounding the orbit scales as  $\hbar$ , tending to zero in the semiclassical limit. A finite intensity enhancement factor affecting an ever smaller region of phase space is entirely consistent with ergodic-

---

\*kaplan@tornado.harvard.edu

†heller@physics.harvard.edu

ity on coarse-grained scales. However, the scarring phenomenon does have very significant effects on physical quantities that depend on fine-scale structure, such as conductances and decay rates through small (or tunneling) leads [7,8].

Another example of markedly non-RMT behavior still consistent with SZCdV coarse-grained ergodicity is found in the “slow ergodic” systems, such as the tilted wall billiard and the sawtooth potential kicked map [9]. In these systems, the classical rate of exploration in momentum space is logarithmically slow, and for large  $\hbar^{-1}$ , the number of channels occupied by a typical eigenstate scales only as  $\hbar^{-1/2} \log \hbar^{-1}$ , constituting an ever decreasing fraction of the  $O(\hbar^{-1})$  total available number of channels. However, the “bright” channels occupied by a given wavefunction tend to be evenly distributed over the entire phase space, and thus coarse-grained ergodicity still holds in the limit, even though the wavefunctions are becoming less and less ergodic at the single channel scale as  $\hbar \rightarrow 0$ . The present paper extends the indications of non-RMT “clumping” of wavefunction density beyond the effects of scarring. Moreover, we use as our examples the original paradigm of classical Hamiltonian chaos, the Sinai billiard, and closely related quantum maps.

The remainder of this paper is organized as follows: in the next section we discuss measures of “microscopic” ( $\hbar$ -scale) quantum ergodicity, including various inverse participation ratios and channel-to-channel transport measures. Then in Section III the connection is made between these stationary properties and the short-time dynamics of a quantum system. In Section IV the Sinai kicked map, a one-dimensional model for the Sinai billiard is introduced and discussed. Strong deviations from single-channel quantum ergodicity are predicted, and distributions for various quantities are computed, that differ greatly from RMT expectations. We see that classical methods can be used to determine the non-ergodic structure of the quantum wavefunctions, even though the classical dynamics is entirely ergodic. Quantitative comparison with numerical data follows in Section V. In Section VI a similar analysis follows for the two-dimensional Sinai billiard system, a paradigm of classical and quantum chaos. Here again strongly non-RMT wavefunction intensity distributions are predicted and observed. In Section VII a simple matrix model is presented and studied, some of the statistical properties of which correspond to those of the Sinai systems. Similarities and differences between the Sinai systems and the matrix ensembles are discussed. In the final section we sum up the results and discuss certain directions for the future.

## II. MEASURES OF $\hbar$ -SCALE ERGODICITY

We now review some important concepts related to the quantitative measurement of quantum structure and transport at “microscopic” (i.e. single-wavelength or

single-channel) scales. An alternative discussion may be found in [9].

Consider a classically ergodic system with quantum eigenstates  $|\xi\rangle$  and a test state basis  $|a\rangle$ . The test basis can be chosen to be the set of position states, momentum states, phase-space Gaussians, or any other set of states motivated by the physics of the problem. Often the test basis will be taken to be the set of eigenstates of a zeroth-order Hamiltonian  $H_0$ , of which the full system Hamiltonian  $H = H_0 + \delta H$  is a perturbation. One is then interested in determining whether the true eigenstates  $|\xi\rangle$  have a nontrivial structure in the states  $|a\rangle$ , or whether the perturbation  $\delta H$  is sufficiently large so as to completely randomize the matrix elements  $\langle a|\xi\rangle$ . Thus, in the case of tight-binding models (e.g. Anderson localization), one may consider  $H_0$  to be the Hamiltonian with on-site energies only, and  $|a\rangle$  to be the position states. The matrix elements  $\langle a|\xi\rangle$  then measure the degree of localization in position space as the hopping matrix elements are turned on. Similarly, in a scattering problem one often finds it useful to use momentum states or channels as the reference basis  $|a\rangle$ , and look for localization of the full eigenstates relative to this basis.

For simplicity, we assume that the classical dynamics given by  $H$  completely mixes the states  $|a\rangle$  with each other, so that no conservation laws prevent each of the eigenstates  $|\xi\rangle$  from having equal overlaps with all of the test states. In the presence of energy conservation or other conserved quantities, the formalism outlined below needs to be modified to take into account constraints imposed by the classical symmetries. This can be done in a straightforward way by, for example, taking the test states  $|a\rangle$  to be coherent states (Gaussians) in phase space. Then it is easy to compute the classical intersection of each such Gaussian with any given energy hypersurface, and the actual quantum intensities  $|\langle a|\xi\rangle|^2$  can be normalized by this classical result. In this way one can easily identify the degree of eigenstate localization (or deviation from ergodicity) due to quantum effects, as opposed to purely classical constraints. See Ref. [10] for a fuller discussion.

We will then focus on the set of (properly normalized) overlap intensities

$$P_{a\xi} = |\langle a|\xi\rangle|^2 \quad (1)$$

to devise measures of “microscopic” localization or ergodicity in the system under study. In RMT (a natural baseline assumption in the absence of dynamical information about our system), the  $\langle a|\xi\rangle$  are predicted to be given by uncorrelated random Gaussian variables, real or complex. The intensities  $P_{a\xi}$  then follow a  $\chi^2$  distribution, of one or two degrees of freedom, respectively. Quantum localization will produce an excess of very large and very small intensities, compared to this baseline result. For convenience, we adopt the normalization where the mean intensity is set to unity:

$$\langle P_{a\xi} \rangle_a = \langle P_{a\xi} \rangle_\xi = 1. \quad (2)$$

Here the averages  $\langle \dots \rangle_\xi$  are taken over all eigenstates  $|\xi\rangle$ :

$$\langle P_{a\xi} \rangle_\xi = \frac{1}{N} \sum_{\xi=1}^N P_{a\xi}, \quad (3)$$

where  $N$  is the total number of states accessible from  $|a\rangle$  (the dimension of the effective Hilbert space). The averaging  $\langle \dots \rangle_a$  over basis states  $|a\rangle$  is defined similarly.

It is often convenient to compress the intensity information into the set of (local) inverse participation values (IPR's) [10]:

$$\text{IPR}_a = P_{aa} = \langle P_{a\xi}^2 \rangle_\xi. \quad (4)$$

$P_{aa}$  is a convenient alternative notation for  $\text{IPR}_a$ , as we will see below when we discuss transport in Eqs. 7 to 11. For a given test state  $|a\rangle$ , the IPR at  $|a\rangle$  gives the first non-trivial moment of the  $P_{a\xi}$  distribution (namely, the ratio of the mean squared intensity to the square of the mean), and thus gives a concise measure of the degree of localization at  $|a\rangle$ <sup>1</sup>. The IPR measures the inverse of the fraction of eigenstates which have significant intensity at  $|a\rangle$ . Thus, equal intensities of all the eigenstates at  $|a\rangle$  would imply  $\text{IPR}_a = 1$ ; this level of ergodicity is of course almost never achieved in a chaotic system. Gaussian random fluctuations (RMT) produce IPR's of 3 (for real overlaps  $\langle a|\xi\rangle$ ) or 2 (for complex overlaps). IPR's exceeding the appropriate baseline value signal the presence of a localization mechanism beyond RMT. In the extreme localization limit where one eigenstate has all its intensity at  $|a\rangle$ , we obtain the maximum possible value,  $\text{IPR}_a = N$ . [A prime example of such extreme behavior is the case of the ‘‘bouncing ball’’ states [12], associated with non-isolated, marginally stable classical periodic motion. Such classical trajectories can trap a quantum wavepacket  $|a\rangle$  for a time comparable to (or even longer than) the time at which individual quantum states are resolved, causing the wavepacket to have  $O(1)$  overlap with only one or a few eigenstates, and leading to  $\text{IPR}_a = O(N)$ . From the SZCdV theorems, we easily see that that the fraction of bouncing ball states must tend to zero in the  $\hbar \rightarrow 0$  limit. This kind of localization is easily visible to the naked eye; other kinds of localization, where the number of eigenstates having intensity at the test state  $|a\rangle$  is large compared to 1 but small compared to the total number of states  $N$ , may be less easy to detect visually but may also be a statistically more important correction to RMT predictions, surviving at arbitrarily small values of  $\hbar$ .]

One can similarly define an eigenstate-specific IPR in the  $|\xi\rangle$ -basis:

---

<sup>1</sup>A slightly different measure of eigenstate localization at a given test state, defined in analogy with classical entropy ideas, is discussed in [11].

$$\text{IPR}_\xi = P_{\xi\xi} = \langle P_{a\xi}^2 \rangle_a, \quad (5)$$

where the average is taken over the test basis  $|a\rangle$ . This of course measures the inverse of the fraction of phase space occupied by a given eigenstate  $|\xi\rangle$ , in the  $|a\rangle$ -basis. A global IPR can also be defined:

$$\text{IPR} = \langle \text{IPR}_a \rangle_a = \langle \text{IPR}_\xi \rangle_\xi. \quad (6)$$

This last quantity measures the inverse fraction of phase space occupied by the *average* eigenstate (or equivalently, the inverse fraction of eigenstates that have intensity at an average location), and can serve as a simple figure of merit for the degree of quantum localization in a given system.

We can relate eigenstate localization to dynamics in the following way. Let

$$A_{aa}(t) = \langle a|e^{-iHt}|a\rangle \quad (7)$$

be the return amplitude for state  $|a\rangle$  to come back to itself after time  $t$ . Given a non-degenerate spectrum, the mean return probability of the state  $|a\rangle$  at long times is proportional to its eigenstate IPR:

$$P_{aa} = N \langle |A_{aa}(t)|^2 \rangle_t, \quad (8)$$

as is easily seen by inserting complete sets of eigenstates on the right hand side. Here the time average on the right hand side of Eq. 8 is taken over times large compared to the Heisenberg time  $T_H$ , i.e.  $\hbar$  over the mean level spacing.

Similarly, we can relate long-time transport to eigenstate correlations. Defining the transport amplitude

$$A_{ab}(t) = \langle a|e^{-iHt}|b\rangle, \quad (9)$$

and a cross-correlation analogous to  $P_{aa}$ ,

$$P_{ab} = \langle P_{a\xi} P_{b\xi} \rangle_\xi, \quad (10)$$

we immediately see

$$P_{ab} = N \langle |A_{ab}(t)|^2 \rangle_t, \quad (11)$$

where again the time average has been taken of the long-time transport probability from  $|b\rangle$  to  $|a\rangle$ . Of course the total probability summed over final states for any given initial state is normalized:

$$\langle P_{ab} \rangle_a = 1 \quad (12)$$

for each  $b$ . The simplest non-trivial quantity which will measure the fluctuation in the probabilities of being in various final states  $|b\rangle$  given an initial state  $|a\rangle$  (or vice versa) is:

$$Q_a = \langle P_{ab}^2 \rangle_b. \quad (13)$$

Roughly speaking,  $Q_a$  measures the inverse fraction of all channels that are accessible at long time from channel  $a$ .

In RMT, all the transport probabilities  $P_{ab}$  are equal to unity with small fluctuations (except for the enhanced return probabilities  $P_{aa} = 2$  or  $3$ ), so  $Q_a = 1$  for each  $|a\rangle$  in the  $N \rightarrow \infty$  semiclassical limit.  $Q_a > 1$  indicates uneven visiting of the available state space starting in the initial state  $|a\rangle$ , and the overall ergodicity of long-time transport can again be summarized in

$$Q = \langle Q_a \rangle_a. \quad (14)$$

In the slow ergodic systems such as the tilted wall billiard and the sawtooth potential kicked map [9], a highly anomalous IPR measure was predicted and observed for small  $\hbar$ , with the system-averaged IPR (Eq. 6) scaling as  $\sqrt{\hbar^{-1}}/\log \hbar^{-1}$ . Semiclassically, the degree of localization in such systems is even stronger, with the IPR scaling as  $\hbar^{-1}/\log \hbar^{-1}$ . The difference is caused by diffraction, which dominates the phase space exploration and increases by  $\sqrt{\hbar^{-1}}$  the fraction of phase space occupied by a typical eigenstate. These same diffractive effects lead to almost perfect long-time transport between channels, with the transport measure  $Q$  an  $\hbar$ -independent constant in the  $\hbar \rightarrow 0$  limit.

### III. SHORT-TIME DYNAMICS AND THE EIGENSTATES

We now discuss the way in which short-time dynamics produces lasting effects on stationary properties, such as eigenstate localization and long-time transport [4,5,10]. Define the local density of states (LDOS) at  $|a\rangle$  as the Fourier transform of the autocorrelation function  $A_{aa}(t)$ :

$$S_a(E) = \frac{N}{2\pi} \int_{-\infty}^{\infty} dt e^{iEt} A_{aa}(t) = \sum_{\xi} P_{a\xi} \delta(E - E_{\xi}). \quad (15)$$

The linearity of the Fourier transform implies that large short-time recurrences in  $A_{aa}(t)$  get “burned into” the spectrum, producing an envelope which must be the smoothed version of the full spectrum  $S_a(E)$ . Thus, let

$$A_{aa}(t) = A_{aa}^{\text{short}}(t) + A_{aa}^{\text{long}}(t). \quad (16)$$

(The most convenient separation between short- and long-time recurrences is situation-dependent, as we will see below.) Then the full spectrum is given by the sum of a short-time envelope and a high-frequency oscillatory structure, coming from the long-time dynamics, that is superimposed on top of that envelope:

$$S_a(E) = S_a^{\text{short}}(E) + S_a^{\text{long}}(E). \quad (17)$$

In the presence of chaos, the number of classical returning trajectories leading from any state  $|a\rangle$  back to itself grows exponentially with time (with some Lyapunov exponent  $\lambda$ ). It is then convenient to classify as “short time” those returns that are governed by one or

a small number of classical paths, and as “long time” those that arise from interference between many classical paths, and for which a statistical description is valid. Due to the exponential proliferation, the dividing line between these regimes is sharply defined in the semiclassical limit  $\hbar \rightarrow 0$ , being given by the mixing time  $T_{\text{mix}} \sim \frac{1}{\lambda} \log \hbar^{-1}$ . Of course, no harm would be done were we to err on the safe side by computing explicitly intermediate-time return amplitudes which could instead have been treated statistically.

Now, in the presence of chaos, the long-time returning amplitude at time  $t$  is expected to fill the initial test state  $|a\rangle$  in a uniform, unbiased way [5], so that the subsequent evolution of this newly returned amplitude is equivalent to the evolution of the original state. More explicitly, we may write for small  $\tau$

$$\begin{aligned} A_{aa}^{\text{long}}(t + \tau) &= \langle a|a(t + \tau)\rangle \\ &= \langle a|a(t)\rangle \langle a(t)|a(t + \tau)\rangle + \dots \\ &= A_{aa}^{\text{long}}(t) A_{aa}^{\text{short}}(\tau) + \dots \end{aligned} \quad (18)$$

Thus, randomly returning amplitude at long time  $t$  leaves its imprint on nearby times  $t + \tau$ , and following [5] we may write the full long-time amplitude to return as a convolution<sup>2</sup>

$$A_{aa}^{\text{long}}(t) = \sum_{\tau} A_{aa}^{\text{rnd}}(t - \tau) A_{aa}^{\text{short}}(\tau), \quad (19)$$

where  $A_{aa}^{\text{rnd}}$  is an uncorrelated Gaussian random variable;

$$\langle A_{aa}^{\text{rnd}*}(t + \Delta) A_{aa}^{\text{rnd}}(t) \rangle = \frac{1}{N} \delta_{\Delta 0}, \quad (20)$$

the averaging being performed over long times  $t$  or over an appropriate ensemble. The  $1/N$  factor provides the right normalization for the probability to return in the absence of nontrivial short-time overlaps, i.e. when  $A_{aa}^{\text{short}}(\tau) = \delta_{\tau 0}$ .

Fourier transforming, the convolution in Eq. 19 leads to multiplication of the smooth short-time envelope by random oscillations in the energy domain:

$$S_a^{\text{long}}(E) = S_a^{\text{short}}(E) S_a^{\text{rnd}}(E). \quad (21)$$

At very long times (beyond the Heisenberg time  $T_H$ , which scales as  $\hbar$  divided by the mean level spacing), the spectrum  $S_a(E)$  becomes resolved into individual spectral lines

---

<sup>2</sup>Discrete-time notation is used here for simplicity and because it is most useful for the repeated scattering situation discussed below. Refer to Ref. [5] for a full treatment of continuous time, which involves introducing an additional very short time scale associated with the initial decay of the wavepacket  $|a\rangle$  (or with  $\hbar$  divided by the energy uncertainty of  $|a\rangle$ ).

$$S_a(E) = \sum_{\xi} r_{a\xi} S_a^{\text{short}}(E) \delta(E - E_{\xi}), \quad (22)$$

where  $r_{a\xi}$  has the statistical properties of a  $\chi^2$  variable.

That is,

$$\langle r_{a\xi} \rangle = 1 \quad \langle r_{a\xi}^2 \rangle = F, \quad (23)$$

where averaging may be performed over eigenstates  $|\xi\rangle$ , test states  $|a\rangle$ , or over an ensemble, and the constant  $F$  is given by 2 or 3, for complex or real eigenstates, respectively. RMT predictions are recovered in the dynamics-free limit  $S_a^{\text{short}}(E) = 1$ ; short-time recurrences cause  $S_a^{\text{short}}(E)$  to vary with energy. This variation in turn leads to larger-than-expected wavefunction intensities  $P_{a\xi}$  at some energies and smaller intensities at others, corresponding to an enhanced IPR and deviation from microscopic ergodicity.

The formalism outlined above has already been used to study the statistical properties of the scarring phenomenon, the anomalous enhancement of certain quantum eigenstates along the unstable periodic orbits of the corresponding classical chaotic system. There, the test state  $|a\rangle$  is a wavepacket launched on or near the classical periodic orbit, and short-time quantum recurrences can be computed analytically (for small  $\hbar$ ) in terms of the monodromy matrix and action of the classical orbit. One finds that the IPR for a test state on the orbit scales inversely with the instability exponent  $\lambda$  of the orbit [5], and the full distribution of wavefunction intensities on and off the orbit can be computed as a function of  $\lambda$  [6]. Averaging over an ensemble of chaotic systems was shown to produce a power-law tail in the intensity distribution, dominated by very strongly scarred states, and in contrast to the exponential tail prediction of RMT. Antiscarred states (ones with anomalously low intensity in certain regions of phase space) are of great importance in open systems: for example, they have been shown to dominate the long-time quantum probability to remain in a classically chaotic system coupled to the outside via a single-channel lead. The size of the effect is exponentially large for small  $\lambda$  [8]. More recently, optimal test states for measuring scarring (“universal scarmometers”) have been developed, which take into account an entire classical orbit and the linearized classical dynamics in its vicinity [13]: they provide larger IPR’s and more evidence of wavefunction localization than do simple Gaussian wavepackets.

## IV. SINAI KICKED MAPS

### A. Definition of system and motivation

The Sinai billiard [14] is a prototypical example of strong classical chaos: it consists of a point particle bouncing freely in a rectangular cavity with hard walls, with a hard disk obstruction placed in the center of the

rectangle. The system has positive entropy classically for any disk size; of course, this fact becomes relevant to the quantum mechanics only in the limit where the quantum wavelength is small compared to the size of the disk. (The mixing time  $T_{\text{mix}}$  after which a typical wavepacket spreads over the entire available phase space is then short compared to the Heisenberg time  $T_H$ , defined as  $\hbar$  over the mean level spacing, at which the quantum dynamics becomes quasi-periodic and individual eigenstates and eigenvalues begin to be resolved.)

The statistics of energy levels in the (desymmetrized) Sinai billiard has been found to be in good agreement with the GOE predictions of random matrix theory [15]. On the other hand, the eigenstate structure of the Sinai billiard turns out to be very different from RMT expectations, and the inclusion of short-time dynamical effects is essential for understanding its quantum ergodic properties. We will return to a detailed discussion of the classical and quantum Sinai billiard in Section VI.

Here we begin with a simplified one-dimensional model which contains most of the important structure of the original two-dimensional system. We notice first that finding eigenstates of a given symmetry class in the Sinai billiard is equivalent to finding the eigenstates in a rectangle one-fourth the original size, with a quarter-circular bump in one of the corners (and possibly with Neumann boundary conditions along one or both of the sides meeting at that corner). We can then imagine finding the eigenstates using an S-matrix approach [16,17], where one considers the scattering of channels of the “free” rectangular system off the quarter-circular bump. The S-matrix has a strong diagonal component due to the straight part of the wall containing the bump, and a complicated off-diagonal structure due to actual scattering off the bump. The long-time dynamics and stationary properties of the system (e.g. eigenstates and eigenvalues) are obtained by iterating the scattering process.

From the surface of section method, we know that Hamiltonian dynamics in a two-dimensional configuration space at fixed energy is dimensionally equivalent to a discrete-time mapping of a one-dimensional system, and can in fact be reduced to such a system. The one-dimensional model we consider in this section is the “Sinai kicked map”, defined on a two-dimensional phase space  $(q, p) \in [0, 1) \times [0, 1)$ :

$$\begin{aligned} p &\rightarrow \tilde{p} = p - V'(q) \bmod 1 \\ q &\rightarrow \tilde{q} = q + \tilde{p} \bmod 1. \end{aligned} \quad (24)$$

The equations of motion Eq. 24 can be viewed as arising from a potential that is periodic in time:

$$H(q, p, t) = \frac{p^2}{2} + V(q) \sum_n \delta(t - n). \quad (25)$$

At the beginning of every time step, the particle is “kicked” by the potential  $V$ , following which the potential is turned off and free evolution takes place for

a unit time interval. The process is then iterated to obtain the long-time behavior. The Sinai billiard's straight wall with a bump has its analogue in the kick potential

$$V(q) = -\frac{K}{2f} \left[ \left( q - \frac{1}{2} \right)^2 - \left( \frac{f}{2} \right)^2 \right] \text{ for } \left| q - \frac{1}{2} \right| < \frac{f}{2}$$

$$= 0 \text{ otherwise,} \quad (26)$$

with a parabolic bump (centered at  $q = 1/2$ ) of spatial extent  $f < 1$ .  $K$  is a constant (which we will set to be of order unity) that determines the typical impulse exerted by the bump. The parabolic shape of the potential bump is chosen for simplicity only; none of the discussion below would be affected if a semicircular or other curved potential were used instead. The key property of the repulsive potential  $V(q)$  is the parameter  $f$ , which sets the fraction of an incoming wave that is scattered classically after one iteration of the map.

The Sinai kicked map is a hard chaotic system with no stable phase space regions (as can be seen easily by computing the Jacobian of the iterated mapping, using the fact that  $V''(q) \leq 0$  everywhere [18]). Like the Sinai billiard (and the Bunimovich stadium), the system has a measure zero set of marginally unstable trajectories, given for example by  $|q - \frac{1}{2}| > \frac{f}{2}$ ,  $p = 0$ . After quantization, such orbits will give rise to “bouncing ball” states [12], which are very strongly localized in momentum space near  $p = 0$ . Our primary interest, however, will be not in this measure zero set of states, but rather in the structure of the “typical” quantum wavefunctions, which obey SZCdV coarse-grained ergodicity, yet have very non-uniform structure at the single channel scale.

The quantization of kicked systems of the form Eq. 24 is straightforward and well-covered in the literature [19]. A value of  $\hbar$  should be chosen so that  $N = 1/2\pi\hbar$ , the number of Planck cells covering the toroidal classical phase space, has an integer value. Then an  $N$ -dimensional position basis for the Hilbert space is given by  $q_i = (i + \epsilon_0)/N$ ,  $i = 0 \dots N - 1$ . Similarly, the momentum space basis is given by  $p_j = (j + \epsilon_1)/N$ ,  $j = 0 \dots N - 1$ .  $\epsilon_{0,1}$  form a family of possible quantization conditions (they correspond to phases associated with circling the torus in the  $p$  and  $q$  directions, respectively). The two bases are related by a discrete Fourier transform. The quantum dynamics is now defined by the unitary  $N \times N$  matrix

$$U = \exp \left[ -i \left( \frac{1}{2} \hat{p}^2 \right) / \hbar \right] \cdot \exp [-iV(\hat{q})/\hbar], \quad (27)$$

where each factor is evaluated in the appropriate basis, and an implicit forward and backward Fourier transform has been performed.

We are now ready to study the structure of the Floquet or scattering eigenstates of the quantum dynamics  $U$ , in the  $p_j$  basis. We notice first that because of the symmetry of the kick potential  $V(q)$  under  $q \rightarrow -q$ , the

classical system has a time reversal symmetry and a parity symmetry:

$$T : t \rightarrow -t, q \rightarrow -q$$

$$P : p \rightarrow -p, q \rightarrow -q. \quad (28)$$

It will be convenient for us to choose a nonzero value for the boundary condition parameter  $\epsilon_1$ , thus breaking the parity symmetry  $P$  under quantization, while maintaining the time reversal symmetry  $T$  by setting  $\epsilon_0 = 0$ . The eigenstates are then real in the momentum basis, and the appropriate RMT baseline is  $\text{IPR} = 3$  (see discussion following Eq. 4). For an asymmetric bump or kick potential, the quantum wavefunction intensity fluctuations would be expected to follow a  $\chi^2$  distribution of two degrees of freedom under RMT, giving rise to the baseline value  $\text{IPR} = 2$ . The analysis to follow is of course completely independent of the symmetry chosen, provided that the appropriate baseline quantum fluctuation factor  $F$  is used.

## B. Short-time dynamics

### 1. Quantum factor of two

As suggested in the preceding section, we should begin our analysis by examining the classical and quantum short time dynamics of the Sinai kicked map in momentum space. In analogy with the quantum return amplitude  $A_{nn}(t)$  of Eq. 7, let  $P_{nn}^{\text{cl}}(t)$  be the classical probability to remain in state  $p_n$  after  $t$  iterations of the map.<sup>3</sup> Classically, for any incoming momentum  $p_n$ , a fraction

$$P_{nn}^{\text{cl}}(1) = 1 - f \quad (29)$$

of all particles remain in momentum  $p_n$  after one kick, while the remaining fraction  $f$  get scattered to other momentum states. Semiclassically, there is an *amplitude*  $1 - f$  for remaining in the incoming channel, as can easily be seen by taking the (semiclassical) overlap of the initial and final states. The *probability* to remain unscattered after one step is then

$$|U_{nn}|^2 = |A_{nn}(1)|^2 = (1 - f)^2. \quad (30)$$

Notice that the quantum one step survival  $|U_{nn}|^2$  is smaller than the classical probability  $P_{nn}^{\text{cl}}(1)$  for not scattering. In analogy to ordinary scattering in free space, one can define a cross section for scattering off the defect. In the limit of small  $f$ , we see from the above analysis that the quantum cross section is twice as large as

---

<sup>3</sup>For conventional reasons we will be using the index  $n$  to label the momentum states instead of the generic index  $a$  used in Section III.

the classical. (This is in complete analogy with quantum scattering theory in free space, in which diffraction results in a quantum cross section twice as big as the classical, even in the short wavelength limit. Essentially, the far-field diffraction into the shadow zone doubles the quantum cross section). Here, there is a quantum probability  $f(1-f)$  for diffracting into *nearby* channels. Classical-quantum correspondence still holds after appropriate coarse-graining over scales large compared to  $\hbar/f$  (but still small classically) in momentum space. As mentioned earlier in our discussion of the Sinai billiard, we are always working in the semiclassical regime  $\hbar \ll f$ , where the bump size is large compared to a wavelength, though it may be small compared to the system size 1.

This difference between the classical and quantum probability to remain in the initial channel ( $(1-f)$  vs.  $(1-f)^2$ ) survives the limit  $\hbar \rightarrow 0$ . In this limit the fraction of diffracted amplitude and the number of scattering channels into which diffraction occurs both remain constant. For finite  $\hbar$ , there will of course be an  $O(\sqrt{\hbar})$  correction to the quantum amplitude  $A_{nn}(1)$ , as it is possible for the horizontal ( $V'(q) = 0$ ) portion of the bump to scatter an incoming channel  $p_n$  back into itself.

## 2. Multistep scattering

We proceed to analyze the multi-step behavior of the dynamics, particularly the probability to remain in the initial state  $p_n$ . In the absence of step-to-step correlation, the classical probability to remain unscattered after 2 steps would be  $P_{nn}^{\text{cl,naive}}(2) = (1-f)^2$ , giving rise to a *quantum* probability  $|A_{nn}^{\text{naive}}(2)|^2 = (1-f)^4$ . This is the same probability that we would obtain by simply iterating the diagonal part of the evolution matrix, i.e. by approximating  $(U^2)_{nn} = \sum_{n'} U_{nn'} U_{n'n} \approx U_{nn} U_{nn}$ . Of course, the true probability to remain in state  $p$  after two steps is  $p$ -dependent: for most values of  $p_n$ , namely  $|p_n| > f$ , entirely different parts of the wavefunction are scattered at each of the two steps, so the classical probability to remain is  $P_{nn}^{\text{cl}}(2) = 1 - 2f < P_{nn}^{\text{cl,naive}}(2)$ . On the other hand, for  $p$  very close to zero, most of the probability that would be scattered at the second step has already been lost on the first scattering event, so  $P_{nn}^{\text{cl}}(2) \approx 1 - f > P_{nn}^{\text{cl,naive}}(2)$ .

The analysis can be extended easily to longer times. The quantum probability to remain after  $t$  steps is still given, to leading order order in  $\hbar$ , by

$$|(U^t)_{nn}|^2 = |A_{nn}(t)|^2 = |P_{nn}^{\text{cl}}(t)|^2, \quad (31)$$

where naively (in the absence of correlations)

$$P_{nn}^{\text{cl,naive}}(t) = (1-f)^t. \quad (32)$$

The true value of  $P_{nn}^{\text{cl}}(t)$  for  $t > 1$  is  $p$ -dependent; in quantum mechanics, this  $p_n$ -dependence can be understood in terms of amplitude that diffracts from  $p_n$  to a

nearby channel in one step and diffracts back into  $p_n$  during a following scattering event. The extra amplitude coming from diffracting back and forth between nearby channels can add in or out of phase with the “naive” contribution. As we found previously, the probability to scatter into a nearby channel after one step is  $f(1-f)$ ; this is comparable to the probability  $f$  for scattering into a classically distant channel and being completely lost from the system as far as the short-time return probability is concerned.

Notice that the short-time return probability of Eq. 31 is completely independent of the shape of the bump  $V(q)$  (as long as the bump amplitude  $K$  is chosen to be  $O(1)$  so as to allow scattering into many distant channels). In fact, we can compute the short time return probability in a simplified model where the non-zero part of the potential is replaced by an absorber, and pieces of the probability density simply get subtracted from the system. For given  $t$ , we then have a distribution of the quantum probabilities to remain  $|A_{nn}(t)|^2$ . We easily see that the *fastest* possible decay of the initial state  $p_n$  is obtained for  $p_n = f$ , where an entirely untouched piece of the wavefunction is absorbed at each step:

$$P_{nn}^{\text{cl,min}}(t) = 1 - tf, \quad (33)$$

for  $t < 1/f$ . The largest values of  $P_{nn}^{\text{cl}}$  arise from  $p_n$  near zero, as described above, and also from  $p_n$  that are near simple fractions like  $1/2$  or  $2/3$ . These slowly-decaying momentum channels give rise to the most non-ergodic long-time quantum behavior, as we shall see below.

For each channel  $p_n$ , then, we can compute the quantum short-time autocorrelation  $A_{nn}(t)$ ; it is given by the square root of the quantum probability to stay (Eq. 31), times the phase accumulated from the (free) quantum dynamics:

$$A_{nn}^{\text{short}}(t) = \langle p_n | U^t | p_n \rangle = e^{-ip_n^2 t/2} P_{nn}^{\text{cl}}(|t|). \quad (34)$$

This holds for both positive and negative short times (note  $A(-t) = A^*(t)$  by unitarity). For a typical momentum  $p_n$ ,  $A_{nn}^{\text{short}}(t)$  has a decay time of  $O(1/f)$ ; upon Fourier transforming we obtain a short-time spectral envelope  $S^{\text{short}}(E)$  centered at quasienergy  $p_n^2/2$  and with width of order  $f$ . Specifically, using the naive estimate of Eq. 32 and taking the bump size  $f$  to be small, we obtain a Lorentzian short-time envelope

$$S_n^{\text{short,naive}}(E) = \frac{2f}{f^2 + \left(E - \frac{p_n^2}{2}\right)^2} \quad (35)$$

for  $\left|E - \frac{p_n^2}{2}\right| \ll 1$ .

## C. Long-time behavior and stationary properties

### 1. Scaling properties

At times long compared with  $1/f$ , most of the initial amplitude in a typical channel  $p_n$  will have been scattered by the bump, and the return amplitude  $A_{nn}^{\text{long}}(t)$  will be given semiclassically by a sum over many nontrivial paths (the relative phases between the paths being of course  $\hbar$ -dependent). As discussed in Section III, and in completely analogy with nonlinear scarring, these long-time recurrences are given by independent Gaussian random variables, convoluted with the short-time dynamics  $A_{nn}^{\text{short}}(t)$ . The full local spectrum  $S_n(E)$  (Eq. 15) is a line spectrum with individual intensities  $P_{n\xi} = N|\langle n|\xi\rangle|^2$  (where we have denoted  $\langle p_n|$  as  $\langle n|$ ) being given by a  $\chi^2$  distribution, weighted by the height of the linear envelope at energies  $E_\xi$ :

$$P_{n\xi} = r_{a\xi} S_n^{\text{short}}(E_\xi). \quad (36)$$

Here  $r_{a\xi}$  are independent  $\chi^2$  variables with mean unity (see Eq. 22). The expected local IPR (Eq. 4) is given by a product of a factor associated with the short-time envelope and a factor ( $F = 3$ ) associated with the spectral fluctuations  $r_{a\xi}$  under the envelope:

$$\text{IPR}_n = 3 \langle (S_n^{\text{short}}(E))^2 \rangle_E = 3 \sum_{t=-\infty}^{+\infty} |A_{nn}^{\text{short}}(t)|^2. \quad (37)$$

Using the naive short-time dynamics of Eq. 32, we obtain an estimate for the typical IPR:

$$\text{IPR}_n^{\text{naive}} = 3 \times \frac{2 - 2f - f^2}{2f - f^2} \approx \frac{3}{f}. \quad (38)$$

Using the upper bound we obtained in Eq. 33 on the rate of short-time decay of an initial momentum channel, we also have a lower bound on the local IPR:

$$\text{IPR}_n^{\text{min}} = 3 \times \frac{2}{3f} = \frac{2}{f} \quad (39)$$

Notice that this lower bound is for moderate  $f$  already larger than the RMT expectation of 3.

For a given value of  $f$ , we may use our knowledge of the short-time classical dynamics and Eqs. 34, 37 to obtain a distribution of the local inverse participation ratios  $\text{IPR}_n$ . For  $f \ll 1$ , the decay time of the classical autocorrelation function  $P_{nn}^{\text{cl}}(t)$  scales with  $1/f$ , so we expect the IPR distribution  $\mathcal{P}_f$  to scale likewise:

$$\mathcal{P}_f(\text{IPR}_n = x) = f \mathcal{P}(fx) \quad (40)$$

for some function  $\mathcal{P}(y)$ . From Eq. 39 we have a lower bound on possible IPR's for small  $f$ , i.e.

$$\mathcal{P}(y) = 0 \text{ for } y < 2. \quad (41)$$

Using the naive estimate of Eq. 38 for the IPR at a ‘‘typical’’ value of the momentum, we determine that the median of the distribution  $\mathcal{P}(y)$  should be in the neighborhood of 3. This discussion of the IPR distribution has

been very general; however the details of the function  $\mathcal{P}(y)$  may in fact depend on classical system parameters other than the bump size  $f$ . For example, in the equations of motion Eq. 24 we could have replaced the free evolution in the second line with

$$q \rightarrow \tilde{q} = q + \alpha \tilde{p} \text{ mod } 1, \quad (42)$$

making the elapsed time  $\alpha$  between kicks an arbitrary parameter. (In the Sinai billiard system, the parameter  $\alpha$  corresponds roughly to the length-to-width ratio of the rectangular billiard.) The detailed properties of the IPR distribution  $\mathcal{P}(y)$  will then depend on the values of classical parameters such as  $\alpha$ , while results such as Eq. 41 apply more generally to the entire class of Sinai-type systems. Below, in Figs. 1 and 2, we present the actual classically computed function  $\mathcal{P}(y)$  for the Sinai kicked map with  $\alpha = 1$ ; there  $\mathcal{P}(y)$  is compared with statistics collected for the corresponding quantum system.

### 2. Tail of the IPR distribution

First, we discuss another important qualitative feature of the IPR distribution, namely the long tail of  $\mathcal{P}(y)$  coming from momentum channels  $p_n$  which are near simple fractions and thus decay on a time scale longer than the typical  $O(1/f)$  steps. Consider a very small initial momentum  $|p_n| \ll f$ . As we saw in the discussion immediately preceding Eq. 31, only a very small fraction of the remaining amplitude in  $|p_n\rangle$  is scattered during each kick following the first one, because the part of the wave which has not yet been scattered shifts very little in position space between kicks. Explicitly, the classical probability (and thus the quantum amplitude) to remain after  $t$  steps is given by

$$|A_{nn}^{\text{short}}(t)| = P_{nn}^{\text{cl}}(t) = 1 - f - (t-1)p_n \quad (43)$$

for  $1 \leq t \leq (1 - f + p_n)/p_n$ . Thus the decay time for the initial state  $|p\rangle$  scales as  $1/p_n$ , and the inverse participation ratio  $\text{IPR}_n$  scales likewise (compare Eq. 37). These IPR's are large compared to the  $O(1/f)$  IPR's obtained for typical channels (yet small compared to the  $O(N)$  IPR's which characterize bouncing ball states).

Similarly, if we choose a momentum channel which lies near a simple fraction,  $p_n = \frac{m}{\ell} + \epsilon$  (for  $\ell\epsilon < f < 1/\ell$ ), then following the first  $\ell$  kicks, a fraction  $\ell\epsilon$  is scattered after each successive kick, and the decay time (and IPR) for such a channel therefore scales as  $1/\ell\epsilon$ . We dub these special momentum channels the ‘‘near-bouncing ball’’ trajectories. We can now easily estimate the fraction of channels with IPR greater than some number  $x$ , where  $x \gg 1/f$ . All channels within  $1/x$  of zero satisfy this condition, as do those within  $1/\ell x$  of a simple fraction  $m/\ell$ . Now we note that for a typical integer  $\ell$ , a finite fraction of integers  $m = 1 \dots \ell$  are relatively prime to  $\ell$ ; thus from each value of  $\ell$  we obtain a fraction



$O(\ell \times \frac{1}{\ell x}) = O(1/x)$  of channels with IPR expected to be greater than  $x$ . Adding up contributions from all values of  $\ell$  between 1 and  $1/f$ , we have a cumulative probability  $O(1/fx)$  for  $\text{IPR}_n$  to be greater than  $x$ , or

$$\mathcal{P}(\text{IPR}_n = x) \sim \frac{1}{fx^2} \quad (44)$$

for  $x \gg 1/f$ . We see that the parameter  $f$  enters in the expected way, and the tail of the scaling distribution (compare Eq. 40) is then given by

$$\mathcal{P}(y) \sim 1/y^2 \quad (45)$$

for  $y \gg 1$ .

### 3. Failure of channel level ergodicity

From the inverse square form of the IPR distribution tail in Eq. 44, it would appear that the mean value of the IPR diverges logarithmically for these systems. However, we notice that at fixed energy the possible IPR is bounded above by the total number of channels  $N$  (this being the IPR for a pure bouncing ball state), and so we have

$$\langle \text{IPR}_n \rangle_n = \langle P_{nn} \rangle \sim \frac{\log N}{f}. \quad (46)$$

We see from Eq. 46 that the mean inverse participation ratio in the kicked Sinai systems diverges logarithmically with increasing energy (or decreasing  $\hbar$ ); thus the wavefunctions are becoming less and less ergodic at the single-channel scale even as the classical limit is approached, despite the ergodicity of the corresponding classical mechanics. The situation is more surprising here than in the slow ergodic systems [9], as in the present case the Lyapunov exponent is positive and the Sinai billiards have long been considered a prototypical example of strong classical ergodicity and mixing. We also note that the logarithmically increasing mean IPR in Eq. 46 is due not to the bouncing ball states (the fraction of these scales as  $1/N$  and thus their contribution to the mean is  $N$ -independent), but rather to the ‘‘near-bouncing ball’’ channels, whose decay time is large compared to the typical decay time  $1/f$  but still small compared to the Heisenberg time  $N$  at which individual eigenstates are resolved. Each such channel contributes to many eigenstates of the system, but only a small fraction of *all* the available eigenstates.

Having made predictions about the structure of the IPR distribution for Sinai-type systems ( $2/f$  lower cutoff,  $O(1/f)$  median,  $O(\frac{\log N}{f})$  mean, inverse square tail), we now proceed to perform a similar analysis for the other statistical quantities discussed in Section II. As discussed previously, the details (factors of order one) of the various distributions and statistical averages will be system-dependent, and can be computed explicitly for

any specific Sinai-type system (as we will do in the following section). What we are interested in here is the universal scaling behavior of wavefunction structure with the bump size  $f$  and the wavelength  $1/N$ .

We consider first the individual wavefunction intensities  $P_{n\xi}$  in the momentum basis. For the typical momentum  $p_n$ , we have seen that the smoothed spectrum  $S_n^{\text{short}}(E)$  has a Lorentzian peak of height scaling as  $1/f$  and width scaling as  $f$ , centered on the optimal energy  $E_n = \frac{1}{2}p_n^2$  (see Eq. 35). Far from  $E_n$ , the smoothed spectrum levels off to a height of order  $f$ , leading to the typical behavior

$$P_{n\xi}^{\text{median}} \sim f. \quad (47)$$

Notice that the median intensity is much smaller than the mean (cf. Eq. 50).

Even for the most anomalously localized channels, the minimum value of  $S_n^{\text{short}}(E)$  never falls below  $O(f)$ ; the smallest values of  $P_{n\xi}$  must therefore arise from  $\chi^2$  fluctuations multiplying this typical intensity. For complex wavefunction amplitudes  $\langle p|\xi \rangle$ , this implies

$$\mathcal{P}(P_{n\xi} = x) \sim \frac{1}{f} \exp(-x/f) \quad [x \ll f], \quad (48)$$

and a corresponding expression is obtained in the real case, where  $P_{n\xi}$  is a  $\chi^2$  variable of mean  $O(f)$  and *one* degree of freedom:

$$\mathcal{P}(P_{n\xi} = x) \sim \frac{\exp(-x/2f)}{\sqrt{2\pi x f}} \quad [x \ll f]. \quad (49)$$

The mean of the intensity distribution is of course fixed by normalization:

$$\langle P_{n\xi} \rangle = 1, \quad (50)$$

where once again the averaging  $\langle \dots \rangle$  can be thought of as an average over eigenstates  $|\xi \rangle$ , momentum channels  $|p_n \rangle$ , or over some ensemble of Sinai-type systems (where e.g. the shape of the bump can be varied while preserving its total size  $f$ ).

### 4. Tails of intensity and transport measures

Lastly, we turn to the tail of the intensity distribution, which we expect to result from large values of the smoothed spectrum  $S^{\text{short}}(E)$ . (Fluctuations of the full spectrum  $S(E)$  around its smoothed value have a  $\chi^2$  form. The probability of obtaining an intensity  $P_{n\xi}$  large compared to the short-time prediction  $S_n^{\text{short}}(E_n)$  is exponentially small.) As previously discussed, a fraction  $O(1/fx)$  of all momentum channels  $|p \rangle$  have a peak in the spectrum  $S_n^{\text{short}}(E)$  of height  $\geq x$ , and the width of such a peak is then  $O(1/x)$ . Therefore a fraction  $O(1/fx^2)$  of all intensities  $P_{n\xi}$  satisfy the condition  $S_n^{\text{short}}(E_n) \geq x$ , and since the fluctuations in  $P_{n\xi}$  around this smoothed value are of order unity, we obtain

$$\mathcal{P}(P_{n\xi} = x) \sim \frac{1}{fx^3} \quad [x \gg \frac{1}{f}]. \quad (51)$$

The eigenstate-basis IPR measure  $\text{IPR}_\xi = P_{\xi\xi}$  (Eq. 5), which measures the inverse fraction of channels in which a given eigenstate lives may be studied in a manner very similar to the channel-basis measure  $\text{IPR}_n = P_{nn}$ . From Eq. 46, we already know the *mean* value of the  $\text{IPR}_\xi$  distribution:

$$\langle \text{IPR}_\xi \rangle = \langle P_{\xi\xi} \rangle \sim \frac{\log N}{f}. \quad (52)$$

We proceed to study the structure of the ‘‘typical’’ wavefunction  $|\xi\rangle$ . From Eq. 51, we know that given some eigenstate  $|\xi\rangle$ , the probability that it has intensity  $\geq x$  at any particular momentum  $|p\rangle$  is  $O(1/fx^2)$ . If we assume the overlaps of  $|\xi\rangle$  with the different momentum states to be uncorrelated, and notice that there are a total of  $N$  momentum channels to overlap with, we see that for  $x \leq \sqrt{N/f}$  there will *generically* be at least one momentum  $|p_n\rangle$  such that  $P_{n\xi} \geq x$ . We now compute the contribution to  $P_{\xi\xi}$  from all intensities  $P_{n\xi} = x$  between  $1/f$  and  $\sqrt{N/f}$ :

$$\begin{aligned} P_{\xi\xi} &= \langle P_{n\xi}^2 \rangle = \int dx x^2 \mathcal{P}(P_{n\xi} = x) \\ &\geq \int_{1/f}^{\sqrt{N/f}} dx x^2 \frac{1}{fx^3} \sim \frac{\log N}{2f} \end{aligned} \quad (53)$$

(recalling  $N \gg 1/f$ ). Thus we see that not only the mean, but also the inverse participation ratio for the *typical* wavefunction tends to infinity in the classical limit:

$$\text{IPR}_\xi^{\text{median}} \sim \frac{\log N}{2f}. \quad (54)$$

The tail of the  $\text{IPR}_n$  distribution arises from the rare intensities  $P_{n\xi} \gg \sqrt{N/f}$ , and using Eq. 51 is easily seen to take the form

$$\mathcal{P}(\text{IPR}_\xi = x) \sim \frac{1}{fx^2}. \quad (55)$$

Having analyzed the statistical structure of individual wavefunctions in Sinai-type systems, we can now proceed to examine the quantum transport behavior. Specifically, we focus on the long-time transport probability  $P_{nn'}$  between two channels  $p_n$  and  $p_{n'}$ , as introduced previously in Eqs. 10, 11. For two *typical* channels  $p_n$  and  $p_{n'}$ , each of the two smoothed local densities of states has the form of a peak of height  $1/f$  and width  $f$  centered around some energy, and then falls off to a value of  $O(f)$  far from that energy (see Eq. 35). Since the two peaks are generically centered at different energies,  $|E_n - E_{n'}| \gg f$ , we easily see that the overlap between the two envelopes is  $O(f)$ :

$$P_{nn'}^{\text{median}} \sim f. \quad (56)$$

Of course we also know the mean value of this distribution by construction:

$$\langle P_{nn'} \rangle = 1. \quad (57)$$

Large values of the transport measure  $P_{nn'}$  arise from those  $p_n$  and  $p_{n'}$  for which the two spectral envelopes  $S_n^{\text{short}}(E)$  and  $S_{n'}^{\text{short}}(E)$  are both anomalously tall and narrow, and which also have significant overlap with each other. Explicitly, in order to obtain a value  $P_{nn'} \geq x$  for large  $x$ , we require  $\text{IPR}_n \geq x$ ,  $\text{IPR}_{n'} \geq x$ , and also  $|E_n - E_{n'}| < \frac{1}{x}$ . The combined probability for these three unlikely events scales as

$$\mathcal{P}(P_{nn'} \geq x) \sim \frac{1}{fx^2} \times \frac{1}{fx^2} \times \frac{1}{x}, \quad (58)$$

so

$$\mathcal{P}(P_{nn'} = x) \sim \frac{1}{f^2x^4} \quad [x \gg \frac{1}{f}]. \quad (59)$$

This is a very quickly decaying tail compared to the one obtained previously for the inverse participation ratio  $P_{nn}$  (compare Eq. 44); thus transport efficiency for this class of systems is much less anomalous than the structure of individual wavefunctions. This makes sense intuitively and is also consistent with the findings for slow ergodic systems in Ref. [9].

Finally, the remaining measure we must consider is the final-state-averaged transport efficiency  $Q_n$  for initial state  $p_n$  (introduced in Eq. 13; see also Eqs. 10, 11 for the definition of  $P_{nn'}$ , the long-time probability of getting to channel  $p_{n'}$  from channel  $p_n$ ). The quantity  $\langle Q_n \rangle$ , as well as the typical value of  $Q_n$ , will be dominated by the Lorentzian envelopes governing typical intensities  $P_{n\xi}$ :

$$\begin{aligned} P_{nn'} &= \frac{1}{N} \sum_{\xi} P_{n\xi} P_{n'\xi} \\ &\sim \int \frac{dE}{2\pi} \left( \frac{2f}{f^2 + (E - p_n^2/2)^2} \right) \left( \frac{2f}{f^2 + (E - p_{n'}^2/2)^2} \right) \\ &= \left( \frac{4f}{4f^2 + (p_n^2/2 - p_{n'}^2/2)^2} \right), \end{aligned} \quad (60)$$

where in the second line we have inserted the typical intensity in channel  $p_n$  of a state  $|\xi\rangle$  with energy  $E$  (from Eq. 35). Now

$$\begin{aligned} Q_n &= \frac{1}{N} \sum_{n'} P_{nn'}^2 \\ &\sim \int \frac{d(p_{n'}^2/2)}{2\pi} \left( \frac{4f}{4f^2 + (p_n^2/2 - p_{n'}^2/2)^2} \right)^2 = \frac{1}{2f}. \end{aligned} \quad (61)$$

The mean and the median both scale as

$$\langle Q_n \rangle \sim Q_n^{\text{median}} \sim \frac{1}{f}; \quad (62)$$

and furthermore in the classical limit  $N \rightarrow \infty$  it is exceedingly difficult to obtain values of  $Q_n$  either small or large compared to  $O(1/f)$ . For *almost any* initial channel  $p_n$ , the fraction of final channels  $p_{n'}$  to which one can

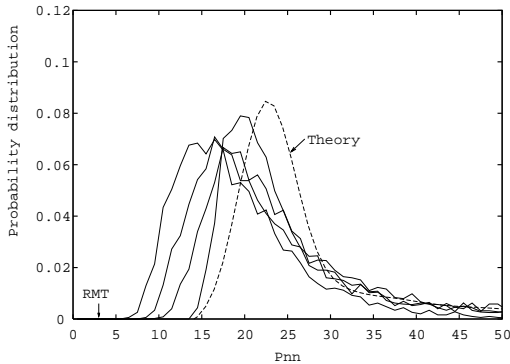


FIG. 1. The distribution of the inverse participation ratio  $\text{IPR}_n = P_{nn}$  is plotted for bump size  $f = 0.1$ . From left to right, the four solid curves represent data for  $N = 100, 200, 400,$  and  $1600$ . The theoretical prediction (see text) is represented by dashes, while the random matrix prediction is  $\text{IPR} = 3$ .

be transported at long times is  $O(f) \ll 1$ . Bouncing-ball (free propagation) channels of course have even less coupling to other momentum states (roughly speaking, they couple to themselves only,  $P_{nn} = O(N)$  and thus  $Q_n = O(N)$ ), but these constitute a vanishing fraction of all channels in the classical limit.

## V. NUMERICAL TESTS IN SINAI KICKED MAPS

We proceed to a numerical study of the structure of wavefunctions in the Sinai kicked systems, focusing on those statistical properties which we have treated theoretically in the preceding section. We begin by considering the distribution of inverse participation ratios  $\text{IPR}_n$  (Eq. 4), each of which measures the inverse fraction of eigenstates having significant intensity at some momentum channel  $p_n$ . The bump size  $f$  is fixed at the moderate value of 0.1, which is small compared to the system size of unity, yet large compared to wavelengths  $1/N \leq 0.01$  which we are going to consider. In Fig. 1, the IPR distribution  $\mathcal{P}_f(\text{IPR}_n)$  is plotted (solid curves) for several values of the quantum wavelength:  $N = 100, 200, 400,$  and  $1600$ . In each case, an ensemble has been constructed by varying the bump height parameter  $K$  in Eq. 26; each realization with  $K = O(1)$  is expected to have the same wavefunction statistical properties, as discussed in the preceding section.

Also plotted as a dashed curve in Fig. 1 is a classical prediction for  $\mathcal{P}_f(\text{IPR}_n)$ . This quantity is obtained by taking a random sample of initial momenta  $p_n$ , and for each of them computing classically the probability  $P_{nn}^{\text{cl}}(t)$  to remain unscattered after  $t$  bounces. Given the short-time classical behavior  $P_{nn}^{\text{cl}}(t)$ , we use Eqs. 34, 37 to predict the expected quantum IPR for that momentum channel  $p_n$ , eventually leading to the distribution shown by the dashed curve. Of course, this is a semi-

classical ( $N \rightarrow \infty$ ) prediction; in particular, it ignores fluctuations in the IPR which result from summing over a finite number of eigenstates in Eq. 4 (even in RMT, fluctuations around the mean value of 3 are expected for finite  $N$ ).

Indeed, we see in Fig. 1 that the quantum IPR distribution does appear to approach the classically predicted distribution as  $N$  gets large; the convergence with  $N$  will be studied more quantitatively below in Fig. 10. By the time we reach  $N = 1600$ , the peak of the distribution is within 10% of the classically expected value, and is shifted by a factor of seven from the naive random matrix prediction. We also notice that *all* the IPR's in our sample are larger than the value of 3 predicted by random matrix theory, and most are larger by a factor of at least five: this is unmistakable evidence of strong deviations from microscopic quantum ergodicity in the kicked Sinai systems.

Next, in Fig. 2 we fix the total number of channels at  $N = 1000$ , and study the IPR distribution for various values of the bump size  $f$ . Guided by the predicted scaling relation of Eq. 40, we choose to plot the distribution of the scaled quantity  $f \cdot \text{IPR}_n$  for each value of bump size  $f$ . For each of  $f = 0.1$  (dashed curves) and  $f = 0.2$  (dotted curves), two distributions are plotted: one for the original kick potential of Eq. 26, and the other for a modified kick potential

$$V(q) = -\frac{K}{2f} \left[ \left( \left| q - \frac{1}{2} \right| + \frac{f}{2} \right)^2 - f^2 \right] \quad \text{for } \left| q - \frac{1}{2} \right| < \frac{f}{2}$$

$$= 0 \quad \text{otherwise.} \quad (63)$$

The latter potential has a kink at  $q = 1/2$ , causing a discontinuity in the classical dynamics. We see from Fig. 2 that the choice of kick potential (Eq. 26 or Eq. 63) has no significant effect on the IPR distribution, as long as the bump size  $f$  is fixed, confirming the universality predicted in the previous section. In particular, we notice that the flat part of the potential [ $V'(q = 1/2) = 0$ ] in Eq. 26, which scatters any incoming channel back into itself, has no discernible effect on quantum localization at the energies under consideration.

The classical prediction for the scaling distribution  $\mathcal{P}(f \cdot \text{IPR})$  is also plotted in Fig. 2 for comparison (see solid curve). We see very good agreement among the 4 sets of quantum data at  $f = 0.1$  and  $f = 0.2$ ; similar scaling behavior with  $f$  is observed for the billiard system in Fig. 9. Again, the slight discrepancy (around 10%) between the numerical data and the classical prediction may be attributed to the finiteness of the energy. At these energies, the minimum observed value of the IPR appears to be near  $1.5/f$ , in contrast to the  $2/f$  semiclassical limit prediction of Eq. 39.

In the tail, we predict (Eq. 44) the inverse square behavior  $\mathcal{P}(x) \approx c/fx^2$  for the IPR distribution, where the constant  $c$  can be determined to be 0.6 through a detailed classical analysis of this system as described above. The

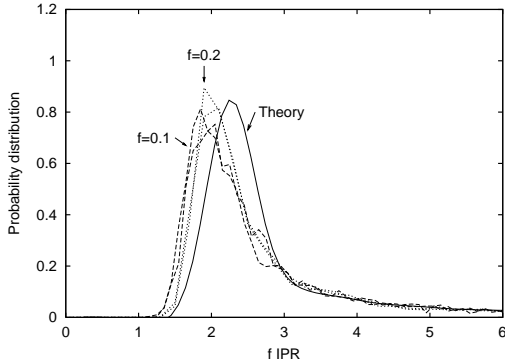


FIG. 2. The distribution of the scaled inverse participation ratio  $f \cdot \text{IPR}$  is plotted for  $f = 0.1$  (dashed curves) and  $f = 0.2$  (dotted curves).  $N = 1000$ , and for each value of  $f$  two distributions are plotted corresponding to different bump shapes (see text).

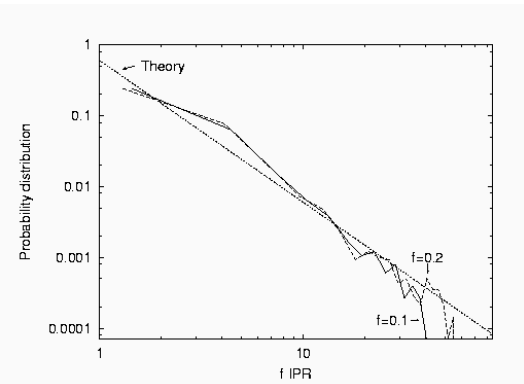


FIG. 3. The tail of the IPR distribution is plotted for  $N = 1000$ , with  $f = 0.1$  (solid curve) and  $f = 0.2$  (dashed curve). The theoretically predicted  $0.6/x^2$  behavior (Eq. 45) appears as a dotted line.

$c/y^2$  tail for  $y = f \cdot \text{IPR}$  is indeed observed in Fig. 3, where the prediction appears as a dotted line on the log-log plot, while the solid and dashed curves represent  $f = 0.1$  and  $f = 0.2$ , respectively. This data was again taken for  $N = 1000$ , and we see the power-law behavior persist to IPR's of about 300, where the IPR becomes comparable to the total number of channels and the theory naturally breaks down.

We recall that this breakdown of the inverse-square law at  $\text{IPR} \sim N$  leads to the prediction of mean IPR growing logarithmically with  $N$ :  $\langle \text{IPR} \rangle \approx 0.6 \log N + \text{const}$  (see Eq. 46). This behavior is indeed observed for  $N$  ranging from 100 to 1000; we omit the figure here because an analogous plot for the billiard system appears in Fig. 10 in the following section. The *median*  $P_{nn}$  shows no such increase with  $N$ ; it saturates at  $\approx 2.35/f$  independent of  $N$  (see Eq. 38). The median IPR for an eigenstate ( $P_{\xi\xi}$ ), on the other hand, does grow logarithmically with  $N$ , but only half as fast as the mean, in agreement with Eq. 54.

We next turn to the distribution of individual wave-

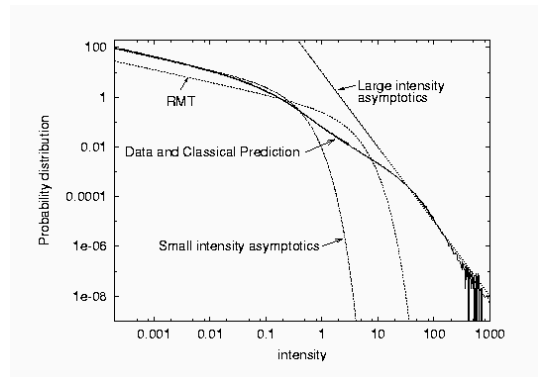


FIG. 4. The distribution of intensities  $P_{n\xi}$  for  $f = 0.1$  and  $N = 1000$  (solid curve). The classical prediction (see text) follows the data very closely (dashed curve). Asymptotics form for the head (Eq. 49) and tail (Eq. 51) of the distribution are both drawn using small dashes. For comparison, the Porter-Thomas distribution of RMT appears as a dotted curve.

function intensities. In Fig. 4 the distribution of intensities  $P_{n\xi}$  is plotted for  $f = 0.1$  and  $N = 1000$  (solid curve). The classical prediction (obtained as described in the discussion of Fig. 1 above) is plotted as a dashed curve; the difference between data and prediction is barely visible except in the very tail where the statistical uncertainty in the data becomes important. The two analytic asymptotic expressions:  $\exp(-x/2f)/\sqrt{2\pi x f}$  for small intensities  $x$  (Eq. 49) and  $1/fx^3$  for large  $x$  (Eq. 51) are also shown in Fig. 4. These two expressions are valid for  $x \ll f$  and  $x \gg 1/f$ , respectively. By contrast, the RMT Porter-Thomas prediction (dotted curve) does not agree with the data in the head, body, or tail of the distribution. See also Figs. 11 and 12, which focus separately on the head and tail of the intensity distribution for the billiard system, and again find good agreement with theory and disagreement with RMT.

The distribution of transport measures  $P_{nn'}$  has also been studied and observed to possess a  $1/f^2 x^4$  behavior for  $x \gg 1/f$ , as predicted in Eq. 59. This data is omitted here as very similar behavior is obtained for the billiard in Fig. 13. The overall transport efficiency  $Q$  has also been studied and follows the predicted scaling  $Q \sim 1/f$  of Eq. 62, so that only a fraction  $O(f)$  of all channels are quantum mechanically accessible at long times starting in any one initial channel.

## VI. LOCALIZATION IN SINAI BILLIARDS

The Sinai billiard was the first nontrivial dynamical system shown to be ergodic with positive Lyapunov exponent [20]. In this sense it is *the* paradigm of chaos. It is also a unit cell of the Lorenz gas, a periodic array of hard disk scatterers (see Fig. 5a).

For numerical reasons we investigate a modified Sinai system with the circular disk off center and jutting only

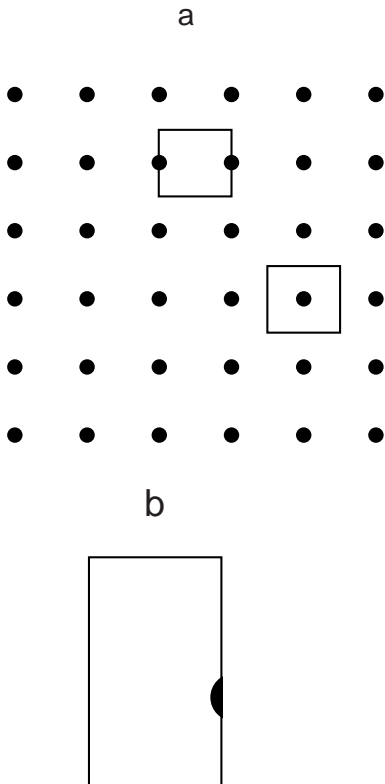


FIG. 5. a) The Lorenz gas and two choices for a fundamental domain. b) A Sinai like billiard related to the Lorenz gas

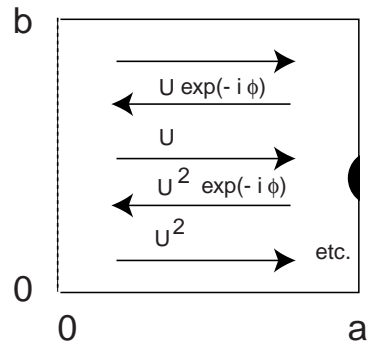


FIG. 6. The modified Sinai system, with a partial disk occupying a variable fraction  $f$  of the right hand vertical wall.

part way into the billiard; this is still a chaotic system (see Fig. 5b).

### A. Scattering method

A scattering system closely connected with both the Lorenz gas and the Sinai billiard puts the Sinai disk at the end of a corridor of length  $a$  (Fig. 6). The scattering wavefunction can then be expanded as

$$\Psi(x, y) = \frac{1}{\sqrt{k_n}} e^{-ik_n x} \sin(n\pi y/b) - \sum_{n'} \frac{1}{\sqrt{k_{n'}}} S_{nn'} e^{-2ik_{n'} a} e^{ik_{n'} x} \sin(n'\pi y/b) \quad (64)$$

where for later convenience we have factored out a phase  $\exp(2ik_{n'} a)$  from the  $n'$ -th column of the S-matrix. (If there is no scatterer on the right hand wall, this makes  $S$  the diagonal unit matrix, assuming Dirichlet conditions there). Now suppose that we reflect the scattered wave from the left wall back towards the right hand side, in accordance with the closed billiard problem we wish to solve. This can be done by imposing a boundary condition at the left wall, which need not necessarily be Dirichlet. (We indicate this by using a dashed line to represent this wall in Fig. 6.) If the wave is reflected from the left wall at  $x = 0$ , it returns with a new phase  $\exp(i\phi)$  given by the boundary condition at the left wall. We define

$$U_{nn'} = S_{nn'} \exp(-2ik_{n'} a + i\phi). \quad (65)$$

Setting  $\psi_n = \exp(-ik_n x) \sin(n\pi y/b) / \sqrt{k_n}$ , the net incoming (right-moving) wave is then

$$(1 + U + U^2 + \dots) \psi_n = \frac{1}{1 - U} \psi_n \quad (66)$$

(see Fig. 6).

Evidently, a bound state can be built up in the billiard if  $U$  has an eigenvalue  $+1$ . We can diagonalize the  $U$ -matrix and consider the properties of its eigenstates. Since  $U$  is a unitary matrix, its eigenvalues lie on the

unit circle. As we change the phase shift  $\phi$  at the left wall, the eigenvalues will correspondingly rotate around the unit circle; each of the  $N$  eigenvalues of  $U$  (assuming there are  $N$  open channels) will pass through  $+1$  for some  $\phi$ , so that *every eigenstate of  $U$  is an eigenstate of the closed billiard with some boundary condition at the left wall and Dirichlet boundary conditions elsewhere.*

If one is willing to search through ranges of energies or of box lengths  $a$  one can find a set of eigenstates satisfying a particular boundary condition; this is a way of finding eigenvalues and eigenstates of the billiard with Dirichlet boundary conditions; they are given by eigenstates of  $U$  with eigenvalue 1 [17,21]. However here we do not seek the Dirichlet solutions, since they are not special as far as their localization in the channel space (this has been tested numerically). This is of great value in gathering the statistics needed here.

Two typical eigenstates of the  $U$ -matrix are shown in Fig. 7; these show fairly obvious non-statistical mixing of different directions of propagation in the billiard (non-mixing of channels in the scattering approach).

### 1. Patterns in the channel (momentum) transport

A new twist arises in the channel transport measure  $P_{nn'}$ , which we now present. Heretofore we have been making the point that Gaussian random wavefunction statistics are much stronger than required for SZCdV ergodicity, and that much coarser randomness can still lead to ergodic transport classically. Below, we see that transport in momentum space may even be highly organized, but in a way that still permits coarse grained SZCdV ergodicity.

The density plot of the transport measure  $P_{nn'}$  for a typical case ( $f = 0.1$  with 280 open channels, side lengths equal) appears at the top of Fig. 8. A pronounced fringe pattern is evident. This pattern changes with the length of the billiard, and as we now show represents alternating constructive and destructive interference due to the phase factors  $\exp[2ik_n a]$  where  $a$  is the box length and  $k_n$  is the horizontal wavevector. The  $S$ -matrix itself shows none of this fringing, but it is strongly evident already for  $S^2$ : We have

$$S_{nn'}^2 = \sum_{n''} S_{nn''} S_{n''n'}, \quad (67)$$

and since  $S$  is diagonally dominated, the major contribution to  $S_{nn'}^2$  for  $n \neq n'$  is

$$S_{nn} S_{nn'} + S_{n'n'} S_{n'n} = S_{n'n'} (S_{nn} + S_{n'n}) \quad (68)$$

Of course  $S_{nn}$  and  $S_{n'n'}$  can interfere; these diagonal elements have factors  $\exp[2ik_n a]$  and  $\exp[2ik_{n'} a]$ , respectively. Subsequent iterations reinforce this interference and give very sharp preferred channels that one can end

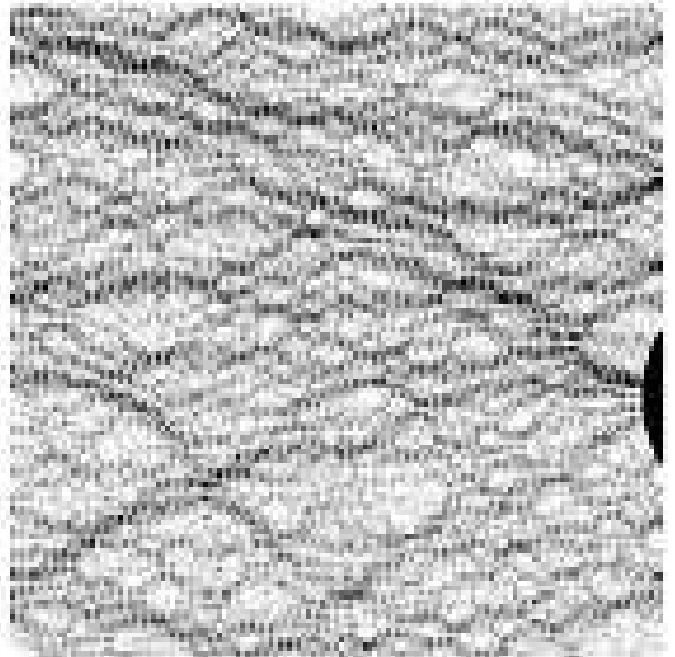
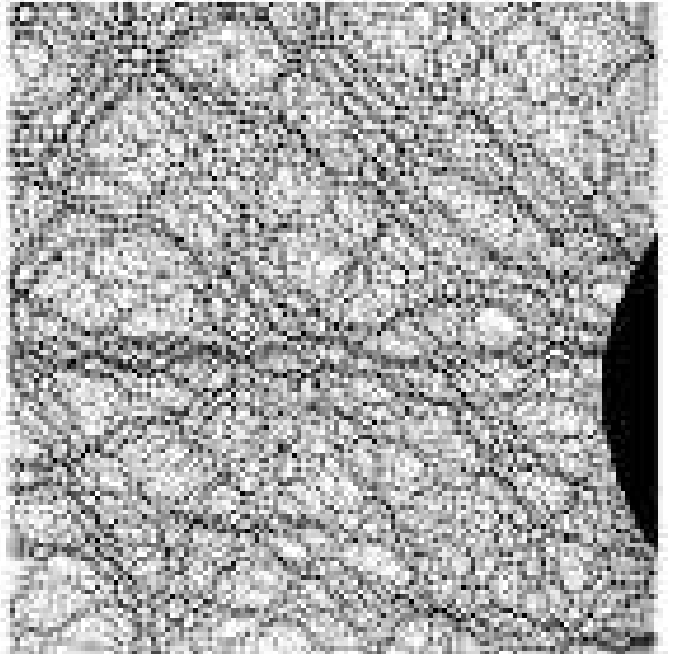


FIG. 7. Two typical eigenstates of the  $S$ -matrix for the Sinai-like scattering system.

up in when starting from a given initial channel. A plot of

$$W_{nn'} \equiv |\exp[2ik_n a] + \exp[2ik_{n'} a]|^{28}$$

appears at the bottom of Fig. 8, and is seen to bear a close resemblance to the fringe pattern in  $P_{nn'}$  (the exponent 28 is of course arbitrary and only serves to set the contrast ratio of the plot). It should be kept in mind that the fine detail (pixel by pixel) of the intensity modulations present in  $P_{nn'}$  are absent in the lower plot, but the overall modulation of the regions of large and small  $P_{nn'}$  are almost identical.

Interestingly, the special channels which correspond to classical free motion (never hitting the obstruction) show up on the diagonal as hyperbolic points of high density. This may be shown by expanding in the channel index (at least in the lower  $n$  region where the Taylor series holds for  $\Delta n \sim 1$ ), e.g.

$$\begin{aligned} & |\exp[2ik_n a] + \exp[2ik_{(n+\Delta n)} a]| \\ & \approx |1 + \exp[2ia (\partial k_n / \partial n) \Delta n]|, \end{aligned} \quad (69)$$

where  $a$  is the length of the rectangular box. Since  $k_n = k_{nx} = \sqrt{2(E - \frac{n^2 \pi^2}{2b^2})}$  and  $k_{ny} = n\pi/b$ , where  $b$  is the height of the box, we have

$$\frac{\partial k_n}{\partial n} = \frac{k_{ny} \pi}{k_n b}. \quad (70)$$

Then the interference in Eq. 69 is maximally constructive for

$$\frac{k_{ny}}{k_n} = \frac{m b}{\Delta n a}, \quad (71)$$

i.e. exactly for the free motion trajectories. The special channels correspond with the hyperbolic regions along the diagonal in Fig. 8. The near-bouncing ball channels near the free propagation channels preferentially diffract symmetrically about these special channels, as evidenced by the local hyperbolic structure. This is again a consequence of the interference structure in Eq. 68. Essentially, there is a preference to scatter by a multiple of a reciprocal “lattice” vector, ( $2a\Delta k = 2m\pi$ ), reminiscent of Bragg scattering from a periodic structure with lattice constant  $a$ .

The dramatic interference pattern is another interesting quantum signature of a short time effect, already evident after one iteration as explained above. It illuminates another variation on the theme of this paper: on scales finer than SZCdV, non-Gaussian statistics may prevail. Here, we see a very structured and nonrandom fringe pattern, which however varies on a scale proportional to  $\hbar$ , doing no harm to the Schnirelman limit.

## B. Numerical method

The simple method which we use to find the  $S$ -matrix makes use of the expansion of Eq. 64, including up to 70

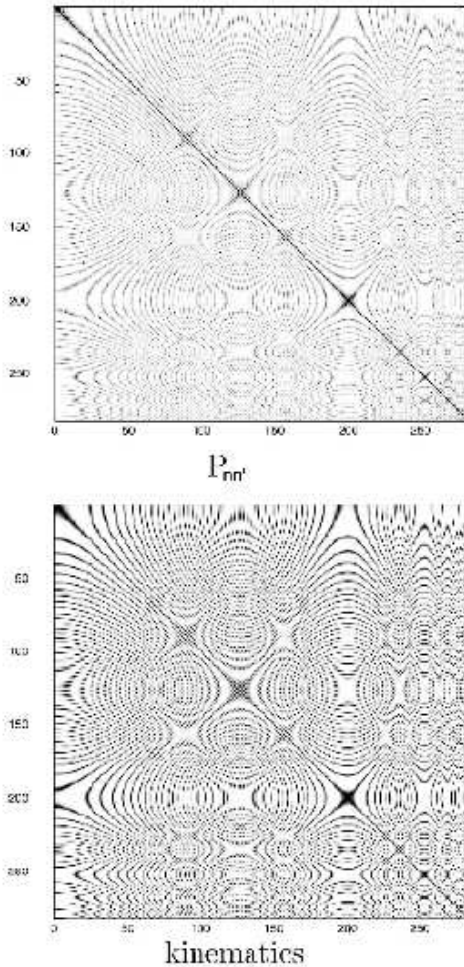


FIG. 8. Top: long-time transport probability between channels  $n$  and  $n'$  for the  $a = b = 2\pi$  (square) billiard,  $f=0.1$  ( $m = \hbar = 1$ ). Bottom: the fringe pattern from Eq. 68.

or 100 closed channels along with all the open channels (50-500 here) as a basis. Linear equations are set up by requiring that  $\Psi(x, y)$  vanish at up to 1000 points  $(x, y)$  along the right hand wall. The basis functions already vanish along  $y = 0$  and  $y = b$ , which is a mixed blessing, since this is also true beyond the right hand wall, where this vanishing is unphysical. Without the inclusion of closed channels the method does not converge. The rectangular linear problem ( $M$  by  $N'$ , where  $N'$  is the total number of channels, including the evanescent modes, and  $M$  is the number of points along the wall set to zero) is then solved by singular value decomposition. The rationale for inclusion of closed channels is that they handle details of the boundary conditions at the disk on a scale smaller than a wavelength. The closed channels are naturally all taken to have total energy equal to the scattering energy, using  $k^2 = k_x^2 + k_y^2$  with  $k_x$  pure imaginary and  $k_x^2 < 0$ . The values of  $k_y$  used were given by the quantized values in the corridor, however this would not be necessary if we included additional points along the top and bottom walls near the right hand end, and explicitly forced the total wavefunction to vanish there.

We find that with the restricted basis described above the convergence is poor if the disk protrudes too far into the billiard. By keeping the center of the disk well to the right of the wall, we are able to get stable results for energies such that  $kd \leq 10\pi$ , where  $d$  is the distance the disk protrudes. This means that the obstruction can be made at least several wavelengths wide in both dimensions, a requirement that we must satisfy in order to be in the high energy regime. Typically the states we study are in the range of the  $10,000^{\text{th}}$  to  $100,000^{\text{th}}$  eigenstate of a fixed boundary condition billiard; it is possible to go beyond the one millionth state for small disks. The range of stability of the method may perhaps be greatly extended by generalizing the basis to more flexible evanescent modes, as discussed above.

The disk covers a fraction  $f$  of the right hand wall. We take that fraction to be between 0.04 and 0.28. In analogy with the map discussed above, a fraction  $1 - f$  of the incoming wave is not scattered on the first bounce, approximately independent of the incoming channel. The discussion of Section IV B holds without modification, including the quantum factor of two in the effective cross section of the disk, corresponding to diffraction into nearby channels.

The localization of the wavefunction which we now have come to expect in channel space ultimately arises from the fact that only a small fraction of the incoming channel is scattered after each iteration of the  $S$ -matrix for small  $f$ . The typical scattering channel presents fresh amplitude to the disk after each bounce, scattering another fraction  $f$  of the remaining amplitude. The resulting slow decay out of the initial channel is already enough to cause gross anomalies in the wavefunction statistics, as compared to RMT. Specifically, this arises from the short-time induced Lorentzian envelope in the

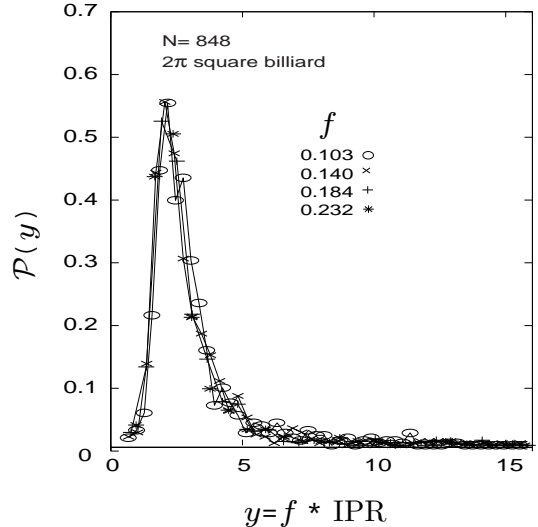


FIG. 9. The probability distribution for the IPR's is plotted for various values of  $f$ , showing the predicted scaling behavior.

quasienergy spectrum, as discussed in Sec. IV B 2.

Classically there are also now a finite number of angles  $\theta$ , with  $(a/b)\tan\theta = n/m$  for integer  $m$  and  $n$ , which never hit the disk. For channels corresponding to propagation near these angles there is a reduction in scattering out of the initial channel. These channels are not true bouncing ball modes, but near enough to have a strong effect on lifetimes. (“Time” is now the number of iterations of the  $U$ -matrix.) Again in complete correspondence with the discussion above, the tails of various distributions are governed by these near-bouncing ball orbits.

### C. Numerical findings—Sinai billiard

We consider first the return probability (inverse participation ratio) measures. The scaling relation  $\mathcal{P}_f(\text{IPR}_n = x) = f\mathcal{P}(fx)$  was predicted in Eq. 40; a plot of  $f\mathcal{P}(fx)$  vs  $fx$  for various values of the disk size  $f$  is shown in Fig. 9, confirming this scaling over the whole domain of IPR values. We see also from the plot that the typical IPR in the Sinai system is  $\approx 2/f$ , which for the values of  $f$  considered is much larger than the RMT-predicted value of 3. We also see the expected broad distribution of IPR's, with  $N$ -independent width, in contrast to the RMT prediction that the spread in the IPR distribution should go to zero as  $1/\sqrt{N}$ .

The tail of the IPR distribution is predicted (Eq. 44) to have the power-law behavior  $\mathcal{P}(\text{IPR}_n = x) \sim 1/fx^2$ . This inverse-square behavior was indeed observed, and is similar to the same falloff already seen in Fig. 3 for the kicked Sinai maps. The power law tail together with the cutoff in the maximum IPR lead to the prediction of Eq. 46, namely  $\langle \text{IPR}_n \rangle_n = \langle P_{nn} \rangle \sim \log N/f$ . A plot



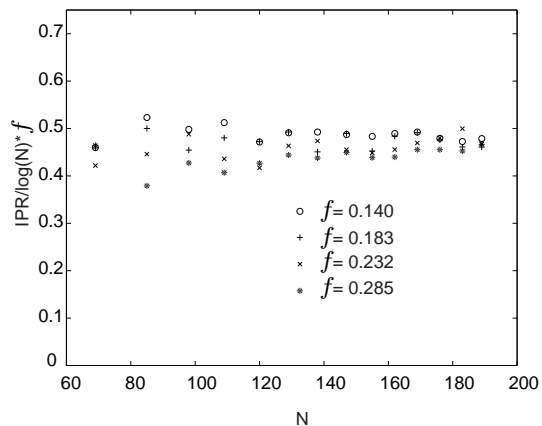


FIG. 10. The average IPR is plotted, showing the predicted dependence on  $N$  and  $f$ .

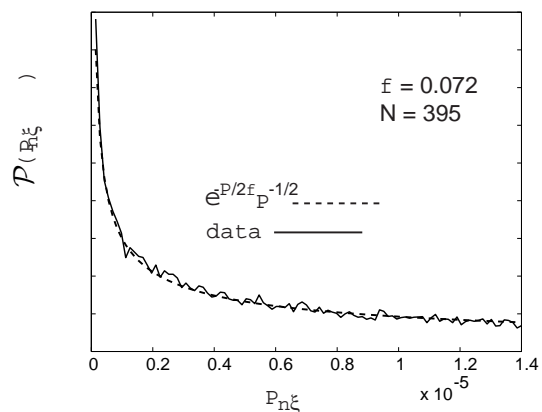


FIG. 11. The distribution of  $P_{n\xi}$  is plotted for small values of  $P_{n\xi}$  and compared with theory, Eq. 49. In this case the bump size is  $f = 0.072$  and the number of channels is  $N = 395$ .

of the the dependence of the average IPR on  $N$  and  $f$  is given in Fig. 10, where the agreement with Eq. 46 is seen to be excellent. As predicted, the mean IPR diverges logarithmically away from its ergodic value of 3 in the classical limit.

The distribution of *small* intensities  $P_{n\xi}$  should be given for our S-matrix by Eq. 49. This behavior at the low end of the  $P_{n\xi}$  distribution is in very good agreement with the theory (Fig. 11).

Finally we consider the tails of the intensity and transport measures. From Eq. 51 we expect a cubic fall off in the tail of the  $P_{n\xi}$  intensity distribution:  $\mathcal{P}(P_{n\xi} = x) \sim 1/fx^3$  for  $x \gg 1/f$ . In Fig. 12 we display the predicted and numerical results, showing good agreement between the two. This behavior is controlled by the near-bouncing ball dynamics. (We do not discuss again the behavior of the intensity distribution intermediate between the head and tail; in Fig. 4 we saw already that the entire distribution is well-predicted classically.)

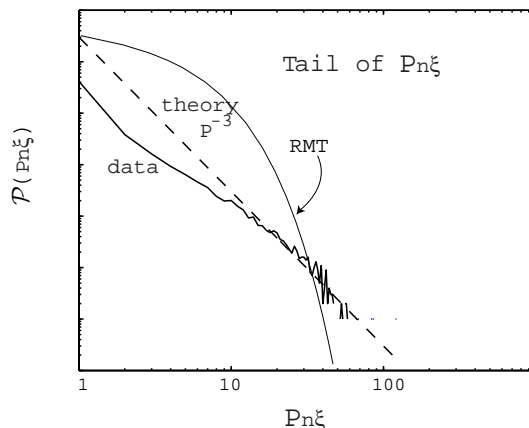


FIG. 12. The tail region of the  $P_{n\xi}$  distribution shows good agreement with the predicted cubic power law, for a  $2\pi \times 2\pi$  billiard,  $f = 0.23$ , 226 channels.

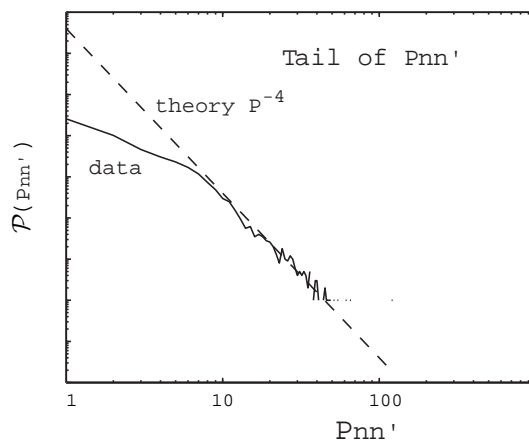


FIG. 13. The tail region of the plot of the  $P_{nn'}$  distribution shows good agreement with the predicted quartic power law, for a  $2\pi \times 2\pi$  billiard,  $f = 0.23$ , 226 channels.

The tail of the transport distribution measure  $\mathcal{P}(P_{nn'})$  is given by Eq. 59,  $\mathcal{P}(P_{nn'} = x) \sim 1/f^2 x^4$ . Fig. 13 again demonstrates very good agreement with this estimate. Notice that the RMT prediction is  $P_{nn'} = 1$  for all channels  $n \neq n'$ .

## VII. SIMPLE UNITARY MATRIX MODEL

The previous examples corresponded to physical systems, or maps, which have a direct basis in dynamics. Above, we have compared the results for such dynamical systems to random matrix theory. However there is a variant of the usual random matrix theory, i.e. a modified random matrix ensemble, which retains some of the gross characteristics of our dynamical systems, while remaining free of any real dynamics. The main idea is to retain the tendency to scatter back into the same channel (diagonal dominance) while making that portion of the amplitude which does scatter do so randomly. This gives rise to Lorentzian envelopes as in the dynamical systems, but not with the near-bouncing ball effects, which strongly skewed the tails of the intensity, IPR, and transport distributions discussed above. The S-matrix for the collision off the Sinai obstruction in the corridor is the key element in the theory of the eigenstates presented above. The S-matrix for this process is unitary and symmetric. The fully random matrix ensemble corresponding to a symmetric S-matrix is Dyson's circular orthogonal ensemble, the COE [22]. However we wish to modify this to a diagonally dominated symmetric unitary matrix  $U$  which includes the effect of random off-diagonal coupling of variable strength. The random component schematically represents the scattering off a small object, with none of the subsequent dynamical correlations built in. We take the form

$$U = \exp[i(D + R)] \quad (72)$$

where  $D$  is a diagonal matrix with randomly chosen quasienergies on the interval  $[0, 2\pi)$ ,  $R$  is a GOE random matrix. Ensembles similar to this have been used previously to model spectral statistics intermediate between Wigner-Dyson and Poisson [23].

For large  $\gamma$  we approach the COE limit; one iteration of the  $U$  matrix on a starting vector will then decorrelate it completely. That is, the self-overlap becomes

$$\frac{|\langle n|U|n\rangle|^2}{|\langle n|n\rangle|^2} \sim \frac{1}{N}. \quad (73)$$

This one step decay corresponds to a pseudoenergy uncertainty of  $2\pi$ , which is just that required to give a uniform spectral density on  $[0, 2\pi)$ . For smaller  $\gamma$  we have slower decay, going as

$$\frac{|\langle n|U^m|n\rangle|^2}{|\langle n|n\rangle|^2} \sim \exp[-2\gamma m], \quad (74)$$

which leads to a Lorentzian lineshape as in Eq. 35.

The measures of distributions, tails, etc. above can be defined for the Lorentzian envelope (modified COE) model as well. The situation here is less rich, since almost all states decay with approximately the same rate, unlike the special channels (angles) in the Sinai models which dictate anomalously slow decay. The IPR is anomalous, up by a factor of  $\sim \gamma^{-1}$  from the RMT prediction due to the Lorentzian LDOS envelopes. Transport is similarly anomalous, with each channel coupled to only a fraction  $\sim \gamma$  of all the other channels at long times ( $Q \sim 1/\gamma$ ).

Due to the near-bouncing-ball orbits, the average IPR in the Sinai systems revealed a localization increasing as  $\log N/f$  as the classical limit  $N \rightarrow \infty$  was taken. For the unitary matrix model, we have only a single decay rate  $\gamma$  (not the distribution caused by the near bouncing ball orbits); the resulting average IPR is therefore predicted to be independent of  $N$ . The decay rate  $\gamma$  is given by the variance of the matrix  $R$  through the Golden Rule,

$$\gamma = 2\pi \langle R^2 \rangle \rho \quad (75)$$

with  $\rho = N/2\pi$ . In the limit of small  $\gamma$ , the IPR should go as  $3 \cdot 2/\gamma$ , where the factor of three is the COE fluctuation factor. The table below shows the mean IPR's averaged over all the basis states for two values each of  $N$  and  $\gamma$  using the modified COE. Excellent agreement is seen between the predicted and found IPR's.

Table of IPR for modified COE			
$\gamma N$	350	450	IPR = $6/\gamma$
0.084	62.6	65.9	IPR = 71.4
0.188	32.9	34.7	IPR = 31.9

The long power-law tails in the intensity, IPR, and transport efficiency distributions, present in the real dynamical Sinai system, are similarly absent in the modified COE model.

## VIII. CONCLUSION

Random matrix ensembles possess eigenstates which are maximally random, consistent with the symmetry constraints which govern the particular ensemble. The properties of such eigenstates form the basis of much work in quantum chaos theory, and more importantly the basis of much theory of nuclei, molecules, and especially mesoscopic devices. Is random matrix theory the limit to which real classically chaotic systems adhere as  $\hbar \rightarrow 0$ ? Definitely not.

The SZCdV theory predicts only coarse grained ergodicity of individual eigenstates in the  $\hbar \rightarrow 0$  limit, which is much weaker than the requirements of random matrix ensembles. This gap, between random matrix ensembles on the one hand and SZCdV on the other, leaves open many questions about the true nature of eigenstates of

classically chaotic systems in the  $\hbar \rightarrow 0$  limit. We have been engaged for some time in the exploration of these questions, which address the fluctuations of eigenstates on scales that shrink as some positive fractional power of Planck's constant (or, more physically, as some negative fractional power of the energy). Since such scales become infinitesimal as  $\hbar \rightarrow 0$ , SZCdV has little to say about them. Yet they may contain infinitely many wavelengths in this limit. The earliest work in this area is scar theory [4,9,13,18], which showed that the effects of the least unstable periodic orbits survive the  $\hbar \rightarrow 0$  limit. However this is only one possible type of a non-RMT "anomaly" in classically chaotic systems.

Our first investigation beyond scar theory, using the so called tilted-wall billiard, examined a very slowly ergodic classical system with the expectation that its eigenstates would be maximally likely to show non-RMT behavior. Indeed the eigenstates did show increasing localization on small scales as  $\hbar \rightarrow 0$ , while still of course obeying the SZCdV ergodic theorem.

In the present study we have switched to the traditional paradigm of classical chaos, namely the Sinai billiard and some close cousins. We have been able to show that the eigenstates are ever more strongly localized in a certain basis as  $\hbar \rightarrow 0$ . The basis used is not extraordinary: essentially it is the usual plane waves (momentum space) of scattering theory. We showed that the mean inverse participation ratio in the Sinai-like systems diverges logarithmically with increasing energy (or decreasing  $\hbar$ ), implying that wavefunctions are becoming less ergodic at the single-channel scale as the classical limit is approached. The situation here is more remarkable than in the tilted billiard [9], since in Sinai systems the Lyapunov exponent is positive and classical correlations decay exponentially. A major conclusion of this work is that the logarithmically increasing mean IPR in Eq. 46 is not due to the bouncing ball states but instead to the "near-bouncing ball" channels, whose decay time is large compared to the typical decay time  $1/f$  but still small compared to the Heisenberg time  $N$  at which individual eigenstates are resolved.

Another key point is that short time quantum dynamics and correlation functions have an irreversible effect on the localization properties of the eigenstates, as in the case of scar theory.

Undoubtedly there are many more non-RMT effects in eigenstates yet to be uncovered in other systems, including some that could affect important physical properties.

## IX. ACKNOWLEDGMENTS

This research was supported by the National Science Foundation under Grant CHE-9610501.

- [1] M. V. Berry, in *Chaotic Behaviour of Deterministic Systems*, ed. by G. Iooss, R. Helleman, and R. Stora (North-Holland 1983) p. 171.
- [2] O. Bohigas, M.-J. Giannoni, and C. Schmit, *J. Physique Lett.* **45**, L-1015 (1984).
- [3] A. I. Schnirelman, *Usp. Mat. Nauk.* **29**, 181 (1974); Y. Colin de Verdiere, *Comm. Math. Phys.* **102**, 497 (1985); S. Zelditch, *Duke Math. J.* **55**, 919 (1987).
- [4] E. J. Heller, *Phys. Rev. Lett.* **53**, 1515 (1984).
- [5] L. Kaplan and E. J. Heller, *Ann. Phys. (N. Y.)* **264**, 171 (1998).
- [6] L. Kaplan, *Phys. Rev. Lett.* **80**, 2582 (1998).
- [7] S. C. Creagh and N. D. Whelan, *Ann. Phys. (N. Y.)* **272**, 196 (1999); *Phys. Rev. Lett.* **77**, 4975 (1996); E. E. Narimanov, N. R. Cerruti, H. U. Baranger, and S. Tomsovic, cond-mat/9812165.
- [8] L. Kaplan, *Phys. Rev.* **E 59**, 5325 (1999).
- [9] L. Kaplan and E. J. Heller, *Physica D* **121**, 1 (1998).
- [10] E. J. Heller, *J. Chem. Phys.* **72**, 1337 (1980); E. J. Heller and M. J. Davis, *J. Phys. Chem.* **86**, 2118 (1982); E. B. Stechel and E. J. Heller, *Ann. Rev. Phys. Chem.* **35**, 563 (1984); E. J. Heller, *Phys. Rev.* **A35**, 1360 (1987).
- [11] B. Mirbach and H. J. Korsch, *Ann. Phys. (N. Y.)* **265**, 80 (1998); *Phys. Rev. Lett.* **75**, 362 (1995).
- [12] J. S. Espinoza Ortiz and A. M. Ozorio de Almeida, *J. Phys. A* **30**, 7301 (1997); A. Bäcker, R. Schubert, and P. Stifter, *J. Phys. A* **30**, 6783 (1997); *Phys. Rev.* **E 57**, 5425 (1998); G. Tanner, *J. Phys. A* **30**, 2863 (1997); M. Sieber, U. Smilansky, S. C. Creagh, and R. G. Littlejohn, *J. Phys. A* **26**, 6217 (1993); P. W. O' Connor and E. J. Heller, *Phys. Rev. Lett.* **61**, 2288 (1988).
- [13] L. Kaplan and E. J. Heller, *Phys. Rev.* **E 59**, 6609 (1999).
- [14] Ya. G. Sinai, *Funct. Anal. Appl.* **2**, 61 and 245 (1968); *Russ. Math. Surv.* **25**, 137 (1970).
- [15] O. Bohigas, M.-J. Giannoni, and C. Schmit, *Phys. Rev. Lett.* **52**, 1 (1984).
- [16] E. Doron and U. Smilansky, *Phys. Rev. Lett.* **68**, 1255 (1992); *Chaos* **2**, 117 (1992); *Nonlinearity* **5**, 1055 (1992).
- [17] H. Schanz and U. Smilansky, *Chaos, Solitons, and Fractals* **5**, 1289 (1995).
- [18] L. Kaplan, *Phys. Rev.* **E 58**, 2983 (1998).
- [19] G. Casati, B. V. Chirikov, F. M. Izrailev, and J. Ford, in *Stochastic Behavior in Classical and Quantum Hamiltonian Systems*, ed. by G. Casati and J. Ford, Springer, New York (1979); M. V. Berry, N. L. Balazs, M. Tabor, and A. Voros, *Ann. Phys. (N. Y.)* **122**, 26 (1979).
- [20] I. P. Cornfeld, S. V. Fomin, and Ya. G. Sinai, *Ergodic Theory* (Springer-Verlag, New York, 1982); L. Bunimovich and Ya. G. Sinai, *Comm. Math. Phys.* **78**, 247 (1980); **78**, 479 (1980); *Erratum*, *ibid.* **107**, 357 (1986).
- [21] E. Bogomolny, *Chaos* **2**, 5 (1992).
- [22] M. L. Mehta, *Random Matrices*, Academic Press (1991).
- [23] T. Guhr, *Ann. Phys. (N. Y.)* **250**, 145 (1996); *Phys. Rev. Lett.* **76**, 2258 (1996); H. Kunz and B. Shapiro, *Phys. Rev.* **E 58**, 400 (1998); F. Leyvraz and T. H. Seligman, *J. Phys. A* **23**, 1555 (1990); G. Lenz, K. Zyczkowski, and D. Saher, *Phys. Rev. A* **44**, 8043 (1991); N. Rosenzweig and C. E. Porter, *Phys. Rev.* **120**, 1698 (1960).